Quasioptical and Physical Optics Design of a Far-Infrared Spatio-Spectral Space Interferometer

C. Bracken[a,*], C. O'Sullivan[a], J.A. Murphy[a], A. Donohoe[a], G. Savini[b], (On behalf of the FISICA Consortium)

[a] *Department of Experimental Physics, Maynooth University, Ireland*
[b] *Department of Physics and Astronomy, University College London, UK*

Abstract

FISICA (Far-Infrared Space Interferometer Critical Assessment) was a three year study aimed at designing a far-infrared spatio-spectral double-Fourier interferometer concept. This paper describes a two-telescope (and hub) baseline optical design, that fulfills the requirements of the FISICA science case. Due the physical size of far-infrared wavelengths with respect to the size of the required optics, a number of different analysis techniques were required for the design work. Approximate simulation tools such as ray tracing and Gaussian beam mode (GBM) methods were employed for initial analysis, with GRASP PO (physical optics) used for final analysis for higher accuracy. The work builds on previous far-infrared double Fourier studies carried out by both European and US institutes, including the ESA Far Infrared Interferometer (FIRI) Technology Reference Study (TRS) [1], The Space Infrared Interferometric Telescope (SPIRIT) study [2] (a candidate NASA Origins Probe mission), and the Balloon Experimental Twin Telescope for Infrared Interferometry (BETTII) [3]. For publications on the broader FISICA project see [4, 5], for example.

Keywords: Far-infrared, FISICA, interferometry, double-Fourier, PyFIInS (Python Far-Infrared Instrument Simulator), optics, quasioptics, PO (Physical optics).

---

1. Introduction

It has been long known that radiation in the far-infrared waveband is related to many important astrophysical processes. However, limitations due to diffraction mean that if resolutions ($\theta_{min} = 1.22\lambda/D$) of less than 1 arc second are to be reached in the far-infrared, then a primary mirror on the order of 50 m must either be built or synthesised. Atmospheric attenuation of far-infrared radiation, and the difficulties involved in using large mirrors in space leads to the requirement of space-based interferometry. Furthermore, if we are to at

---

[*] I am corresponding author
Email address: `colm.bracken@nuim.ie` (C. Bracken)
URL: `https://www.maynoothuniversity.ie/experimental-physics/our-people/colm-bracken` (C. Bracken)

least match the spectral resolution of single dish far infrared observatories such as Herschel [6, 7], Spitzer [8] and SPICA [9], then a high resolution spectroscopic technique must be used in combination with the spatial interferometer. The technique selected for the FISICA study was Fourier transform spectroscopy (FTS), and when spatial and spectral methods are used together the technique is called double Fourier spatio-spectral interferometry [10].

One of the main drivers for a baseline optical layout for a far-infrared double Fourier space interferometer was the production of realistic aperture fields for use with the recently developed PyFIInS (Python Far-infrared Interferometer Instrument Simulator) [11, 12]. The PyFIInS simulator has thus far been capable of modeling the double Fourier interferometry process, and reproducing sample sky maps while accounting for realistic sources of error and noise. To date though, the input primary mirror beams on the sky were those of uniformly illuminated apertures, and thus did not take account of optical aberrations, beam structure and polarisation effects of realistic detector beams, etc. Furthermore, it was clear that at such long wavelengths and propagation distances, diffraction would cause difficulties.

2. Light collecting telescopes

In the context of the FISICA study, the demands on sensitivity, resolution, and FOV were well defined by the science case, and these requirements drove the initial optical design parameters. 2 m primary mirrors (flux collectors) are required if integration times are to be kept within practical timescales. For example, for an interferometer with two mirrors ($d = 2$ m), the average time needed per-pointing is 33 hours. This corresponds to approximately 4000 u-v sample points with 2 FTS scans per pair of u-v points [13]. The most demanding science questions translate into the need to spatially resolve astrophysical objects of angular size ≈ 0.1 - 0.25 arcseconds at wavelengths ranging from 25 to 200 μm, with a desire to extend the range to 400 μm. This sharp resolution at such long wavelengths requires interferometric baselines up to $B = 100$ m [13, 4]. The wide spectral coverage would be separated into three wavebands: 1) $25 - 50$ μm, 2) $50 - 100$ μm, 3) $100 - 200$ μm, with a possible 4th band of 200 to 400 μm, if feasible. Finally, science questions relating to mapping of the galactic centre call for a 1 arcmin^2 FOV. One on-axis single-mode coherent detector/horn assembly illuminating a 2 m primary mirror will yield a beam size on the sky on the order of a few arc seconds squared. However, filling the relatively large arcmin^2 FOV with one such detector is not realistic, and so a FPA (focal plane array) of single-mode or over-moded horns will be required. Thus, these values of $d = 2$ m, $B = 100$ m, FOV = $(\pm 0.5')^2$, and the need for a FPA provided a clear starting point for the optical design.

Somewhat different to imaging telescopes, the purpose of the light collecting telescopes in this instance is to convert a collimated beam into a smaller collimated beam with a de-magnified beam radius. However, the same desire to maintain a low level of aberration and good imaging properties still exists for such an afocal system. In fact, there is a much tighter tolerance on wavefront errors in an interferometer system, as fringe visibility can be greatly affected by both surface form errors and random surface roughness [14].

The beams from the primary mirrors will have to be de-magnified to keep the size of the cooled hub optics small. Also, the beams must be propagated over distances up to $B_{1/2} = 50$

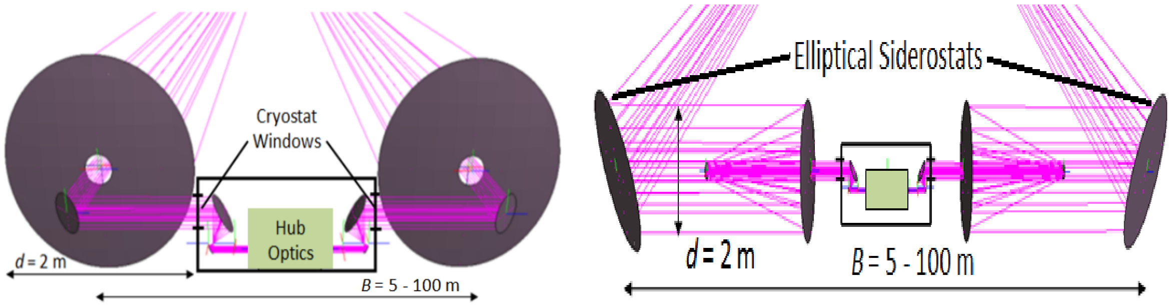

Figure 1: Screen shot of GRASP PO models of interferometer concept designs where de-magnification is carried out before propagation over the semi-baseline (left), and after propagation (right). The required dimensions of the elliptical siderostats in the right figure are $a = 2$ m and $b = 2.83$ m.

m, before being combined in the hub craft. For each of the two beam paths a flat mirror oriented at 45° to both the sky and the hub spacecraft is used to steer the beam toward the hub. De-magnification of the beams can be performed either before or after propagation over the semi-baseline. Figure 1 (left) shows a design where de-magnification is done before propagation over $B_{1/2}$. This was the option chosen by the FIRI study [15, 1], where two on-axis afocal telescopes (pointed at the source) sample the u-v plane and de-magnify the aperture fields. A small flat elliptical mirror then steers the condensed beam toward the hub. Figure 1 (right) illustrates how de-magnification can alternatively be done after propagation over $B_{1/2}$, as selected by the balloon-borne BETTII mission [3] (due for launch in 2016). In this case two large elliptical flat siderostats (oriented at 45° to the source) sample the u-v plane and propagate the large beams toward the hub. Two afocal telescopes (off-axis systems for BETTII) close to the hub then de-magnify the beams before they enter the hub.

2.1. Trade-off analysis

It was decided to compare optical designs where de-magnification is carried out at the primary flux collectors (which we will call type 1) with those where de-magnification is carried out close to the hub (we will call type 2). Using the ray tracing software Zemax, the predicted beam sizes at the hub cryostat window were compared for type 1 and type 2 designs. To be sure of comparing like-with-like, the analysis assumed the same parameters for the condensing optics in each case, namely de-magnification of $m = 10$ and $F/1.5$ primary.

Based on these preliminary geometrical models it was quickly realised that there are significant differences for type 1 and type 2 systems, in terms of the minimum beam sizes at the hub. For type 1 designs, limiting the size of the primary mirrors to 2 m for a FOV of $(\pm 0.5')^2$ results in very large beam cross-sections at the hub window (over 400 mm). This is simply due to a 'lever-arm' effect on the off-axis rays, where the propagation angles (ϕ_f) are magnified as $\phi_f = m\phi_i$, where ϕ_i are the angles of incidence (Figure 2 (top left)).

Given that the aperture to the hub cryostat must be cooled, its size should thus be kept as small as possible. If then, the cryostat window is to be the limiting factor, and the hub beam diameter is set to, say, 200 mm, we find that the lever-arm effect demands the expansion of the primary mirrors to a diameter of at least 3.5 m (or even larger if there is to

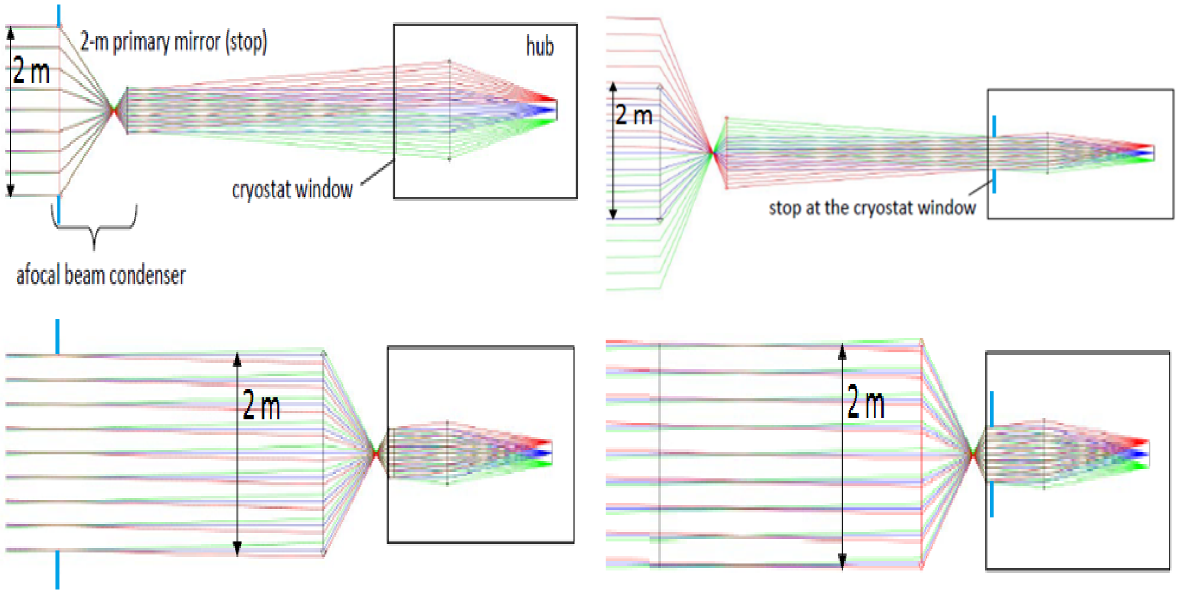

Figure 2: Equivalent lens models (for clarity) of four of the many possible interferometer optical layouts (not to scale). The top two are systems where de-magnification is performed before propagation over the baseline, and the bottom two are systems where de-magnification is performed before propagation. For both types the optical stop was placed at the 2 m primary mirror (left), and then at the cryostat window on the hub (right). Images are not to scale.

be no truncation of the longer wavelengths at the cryostat window) (Figure 2 (top right)). There are of course enumerable compromise options within (and beyond) the two extremes just described for a type 1 layout, and the exact design of a type 1 system will need to consider a trade-off between primary mirror size vs. cryostat window size.

In contrast to the type 1 design, if de-magnification is instead carried out close to the hub (type 2), a relatively small beam diameter at the hub cryostat window is achievable without increasing the size of the primary mirror. There is of course the addition of a large siderostat for each beam path, thus significantly increasing the mass of optical components required. As would be expected, due to the short distance between the telescope and hub for a type 2 design, there is little difference between placing the optical stop at the telescope primary mirror or at the hub window, unless a significantly smaller window is required. A summary of design conclusions is given in Table 1.

A broader trade-off analysis of various telescope types such as Gregorian vs. Cassegrain, and on-axis vs. off-axis (for a range of F/#'s) was reported on in a previous paper [14]. Ultimately, the final design for a particular mission will be decided upon based on mass and compactness considerations vs. sensitivity and wavefront quality, etc. For the purposes of the current work, one design option was selected for further study, though the same analysis techniques could be applied to any of the above mentioned formats. Given that FISICA was a study of a space-based system, and since mass limitations imposed by launch will likely exclude a type 2 design, it was a type 1 design that was selected for detailed

De-mag. at primary Stop at primary	Very large cryostat window ($>$ 400 mm)	2 m primary (minimum mirror requirement)
De-mag. at primary Stop at cryostat	Quite large cryostat window (200 mm for $m = 10$)	Large 3.5 m primary
De-mag. at hub Stop at primary	Moderate cryostat window requirement (100 mm)	2 m primary, plus elliptical siderostat $a = 2$ m, $b \approx 2.8$ m
De-mag. at hub Stop at cryostat	Smallest cryostat window requirement (70 mm)	2.8 m primary, plus elliptical siderostat $a = 2.8$ m, $b \approx 3.9$ m

Table 1: Summary of the various optical formats for a two-telescope interferometer, and the implications.

modeling, beginning with a simple Gaussian beam analysis. This Gaussian beam model is approximate, in that it accounts for beam divergence, but neglects diffraction effects.

2.2. Optimising baseline telescope design

The primary mirror of the chosen format was set to 2 m (stop placed at primary), meaning that the cryostat window will need to be large. However another compromise option that would reduce its size would be to accept a reduced FOV (see Figure 3 (right)). Again, these are details that would be refined for a real system design in the future.

As well as the angular magnification of off-axis rays due to m (described above), significant beam spreading due to diffraction can also occur at the longer wavelengths if the beams are condensed too much. To this end, analysis was carried out to determine the best value for m from both a geometrical and diffractive point of view. The wavelength range considered was 20 to 200 microns in steps of 20 μm, as well as 400 μm (possible extension in spectral coverage, if feasible).

The on-axis beam from each of the telescopes can be approximated as a Gaussian [16] with beam width w that varies with propagation distance z, as shown in (1).

$$w(z) = w_0\sqrt{1 + \left(\frac{\lambda z}{\pi w_0^2}\right)^2} \tag{1}$$

where λ is the wavelength of the light, and w_0 is the radius of the de-magnified beam before propagation over the length of the baseline. However, the relatively large field of view required by the FISICA science case means that the most extreme off-axis rays should also be considered. When the off-axis fields - incident at angles $\phi = \pm 0.5'$ - are de-magnified by m, they too can be treated as simple Gaussian beams, but propagating at angles $m\phi$. The result is Gaussian field distributions with offset (Δw) from bore-sight, as described by (2).

$$D(z) = w(z) + \Delta w = w_0\sqrt{1 + \left(\frac{\lambda z}{\pi w_0^2}\right)^2} + z\sin(m\phi) \tag{2}$$

If we then consider that the field intercepted by the primary mirror can be represented by a uniform disk of radius $a = 1$ m, and that the best fit Gaussian to a uniform disk of radius a has a beam radius of $0.892a$, then the best fit Gaussian to a primary mirror of radius = 1 m has a beam radius of 0.892 m. Figure 3 (left) shows how beam size increases with propagation distance for a range of initial beam width values. In this case λ was set to 200 μm since beam divergence will clearly be more severe at the longer wavelengths. As shown, the minimum beam width that can be achieved at the hub for the maximum baseline is about 173 mm, which corresponds to an initial beam width of about 89 mm, or a de-magnification of $m = 0.892/0.089 = 10$.

Figure 3 (right) shows the minimum beam width that can be achieved at the hub for increasing de-magnification and for a variety of wavelengths. In this case the propagation distance was set to the maximum semi-baseline ($B_{1/2} = 50$ m). Figure 3 (right) also shows results for $\lambda = 400$ μm, where it is clear that extending the spectral coverage to this range will significantly increase the minimum beam size at the hub. On the other hand, if a smaller field of view is to be accepted (lowermost curves labeled λ^*), then a significantly smaller beam size can be achieved at the hub, even for wavelengths up to 400 μm. The smallest beam possible will clearly be for an on-axis field only, resulting in a beam radius at the hub (for $\lambda = 200$ μm) of 79.8 mm (not shown in Figure 3). This optimised value corresponds to a beam at the telescope secondary mirror with a beam waist of $w_0 = 56.4$ mm, or de-magnification $m = 892/56.4 = 15.8$. However, this scenario corresponds only to on-axis plane wave illumination, i.e. a single on-axis point source on the sky.

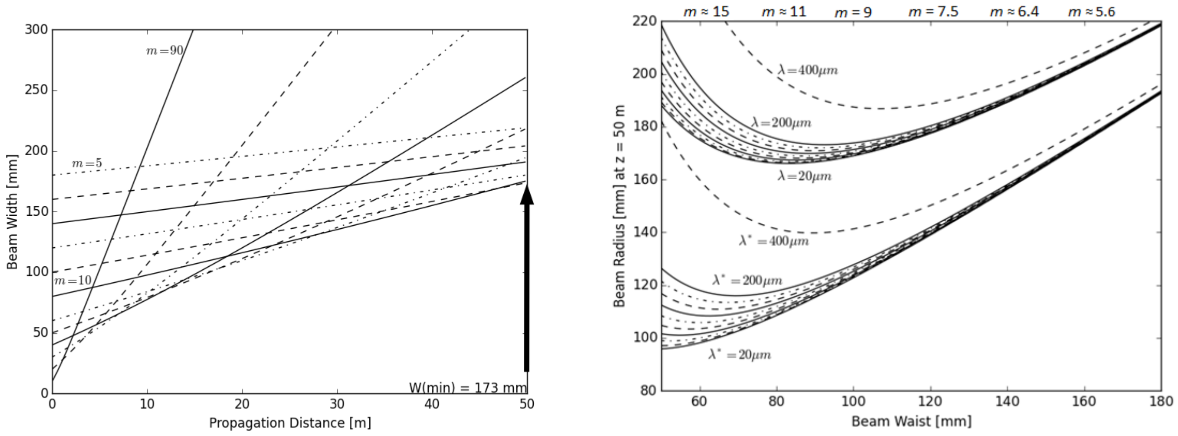

Figure 3: Beam radius (including off-axis beams) as a function of propagation distance for different beam waists at collecting telescopes for $\lambda = 200$ μm (left), and beam radius at hub telescope for baseline of $z = 50$ m for various wavelengths ranging from 20-200 μm (in steps of 20 μm), and 400 μm (right). The lower curves (indicated by λ^*) correspond to the same wavelength values, but for a reduced FOV of $\pm 0.33'$.

3. Hub Optics

3.1. Hub propagation

Based on the analysis described above, a cryostat window diameter of 400 mm was selected, with some level of truncation expected at the longest wavelengths. Following propagation across the variable baseline, and entry into the hub, the beams require further de-magnification so as to minimise the size of the cooled optical components within the hub. An off-axis Gregorian-like design with primary mirror diameter of 400 mm was chosen, which relied on the heritage from the FIRI study [15]. Table 2 shows the parameters for both the light collecting telescopes and the hub condensing optics.

Primary Telescopes (Cassegrain afocal)	Focal Length [m]	De-magnification (f_1/f_2)	Mirror Radius [m]	$F/\#$	Conic Const.
Primary (M1)	3	10	1	1.5	-1
Secondary (M2)	0.3		0.1	1.5	-1
Hub Condensers (Gregorian afocal)	Focal Length [m]	De-magnification (f_3/f_4)	Mirror Radius [m]	$F/\#$	Conic Const.
Primary (M3)	0.2	5	0.20	0.5	-1
Secondary (M4)	0.04		0.043	0.465	-1

Table 2: Parameters of both the light collecting telescopes and hub condensers.

Following de-magnification by the hub condensers, the beams - now approximately 30 mm in radius - are propagated through a series of optical elements including beam splitters, dichroics, rooftop mirrors, and for one arm the FTS (Fourier transform spectrometer). Following combination of the two beams with a final beam combiner, the signal will be focused onto the focal plane array by a final off-axis mirror. The mirror was given a focal length of 250 mm and angle of throw of 45°, and positioned 3 m from the hub window to allow for a realistic optical path length to facilitate all of the instrument specific optical elements. For the purposes of the current work, the final hub mirror was simply given an over-sized radius of 600 mm to ensure a low level of truncation at all wavelengths. No attention is given here to the specifics of the other internal hub optics, since a number of optical layouts could be chosen for a range of science instruments based on heritage from the Herschel Space Observatory [17, 18, 19], or indeed the research to date on the planned SPICA mission [20, 21]. What is certain though, is that the design of the hub optics for a future mission will require great care if beam truncation is to be minimised. Given the FOV required by the FISICA science case, and the resulting very large hub beams for wavelengths beyond about 200 μm, band 4 is ignored from this point as it will likely be unfeasible for a FISICA-type system.

3.2. Focal plane fields and detector array

Using the GRASP 9.1 PO package [22], a total of nine plane waves - all linearly ploarised in x - were propagated through the full system, from the primary flux collectors to the focal plane (Figure 4 (left)). The first plane wave represented an on-axis field, and the remaining eight corresponded to the limits of the FOV in $\theta = \pm 0.5'$, $\phi = \pm 0.5'$, and (θ, ϕ) = $(\pm 0.5', \pm 0.5')$. Figure 4 (right) shows a mosaic of the 9 fields on the focal plane for $\lambda = 200\mu$m, at which the beams would be expected to suffer the most significant level of diffraction and thus largest spot sizes. The filled band 3 FPA would consist of a 5 × 5 detector array. Band 2 would likely consist of a 10 × 10 array, and band 1 a 20 × 20 array.

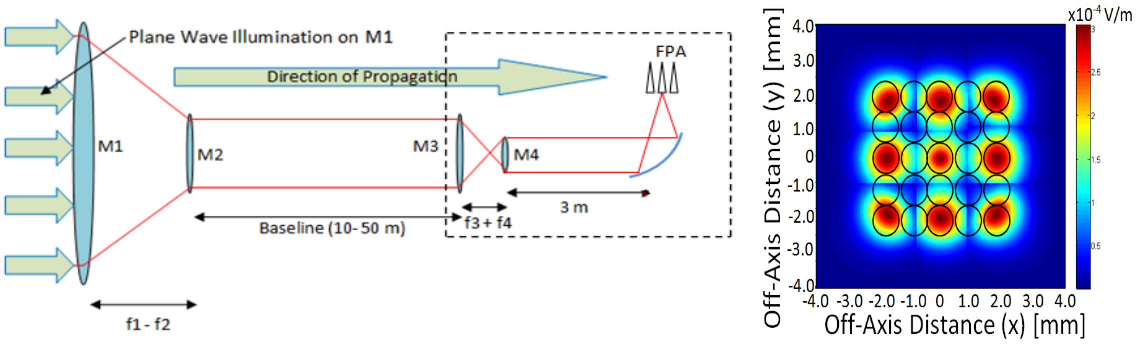

Figure 4: Lens equivalent model (not to scale) of the full optical system for one of the two beam paths (excluding instrument-specific elements). The dashed boxed-off section corresponds to the hub optics (left). Focal plane fields for plane wave illumination of the 2 m flux collectors, with footprint of feed horn array superimposed (right). Each horn aperture footprint corresponds to the horn mouth of radius $a = 0.375$ mm.

4. Detector to sky propagation

In the context of simulating a detector beam for propagation through the interferometer system, no concern was given to the particular type of detector. A number of detector technologies would suit the FISICA sensitivity and bandwidth needs, with the leading technologies being TES's (transition edge sensors) and KID's (kinetic inductance devices). TES's currently have a higher TRL (technology readiness level) [23], but there is a lot of promise for the future of KID's [24] for a FISICA-type system. For the purposes of the current work, smooth walled, conical horns of length $L = 4.0$ mm and aperture $a = 0.375$ mm (see Figure 4 (right)) were positioned on the focal plane in the PO model. The horns were fed by cylindrical waveguides of radius $b = 60$ μm, giving a cut-off frequency of just over 200 μm. A TE_{11} transverse electric waveguide mode was excited at the aperture of each waveguide. Each corresponding horn aperture field was then split into two beams, and each beam was propagated through one of the two beam paths of the interferometer and on to the sky.

4.1. Beams on the sky

Figure 5 shows cuts through the far-field radiation patterns of a single telescope primary mirror corresponding to one of the two beam paths (no interferometry). The results for the on-axis pixel (Figure 5 (top)) show no significant change in the far-field pattern with changing semi-baseline distance. In fact, there is a slight increase in on-axis gain for the *longer* semi-baseline. This counter-intuitive result can possibly be explained by calculating the Fresnel number ($F = a^2/L\lambda$) for the system at the different baseline values. At the shorter semi-baselines the hub is still in the near-field of the light collecting telescopes (see near-field (or Fresnel) diffraction [25, 26]). This means that the beam evolves in a much more complicated manner as it propagates, compared to the more simple far-field beam divergence that is directly proportional to propagation distance (see far-field (or Fraunhofer) diffraction [27]). At all baseline values, the clear increase in on-axis gain at the shorter wavelengths is to be expected, as would be the case for a conventional radiating single mirror/dish.

The results for the furthest off-axis pixel (Figure 5 (bottom)) show a small decrease (about 1 dB) in gain for $B_{1/2} = 50$ m compared to $B_{1/2} = 5$ m, which indicates some level of beam truncation at longer baselines. In fact the relative decrease is the same for $\lambda = 200$ μm and $\lambda = 100$ μm, indicating the truncation is primarily a result of the off-axis lever-arm effect, rather than diffraction which would be wavelength dependent. Figure 6 again shows the single telescope far-field pattens, but for varying hub mirror diameter. Clearly the choice of $d_3 = 400$ mm ($M3$ mirror radius of 0.2 m (Table 2)) provides a relatively low level of beam truncation (about 1dB) compared to a completely over-sized mirror. However, for 99% coupling at all wavelengths and for all pixels, a hub mirror of 430 mm would be required.

In terms of input for the PyFIInS instrument simulator then, separate beam data were generated for three wavelengths corresponding to the start, centre, and end of band 3 ($\lambda = 100, 150$, and 200 μm), and three baselines ($B = 10, 50$, and 100 m). Based on these sample beams, the simulator then interpolates beam patterns for a larger number of wavelength and baseline samples.

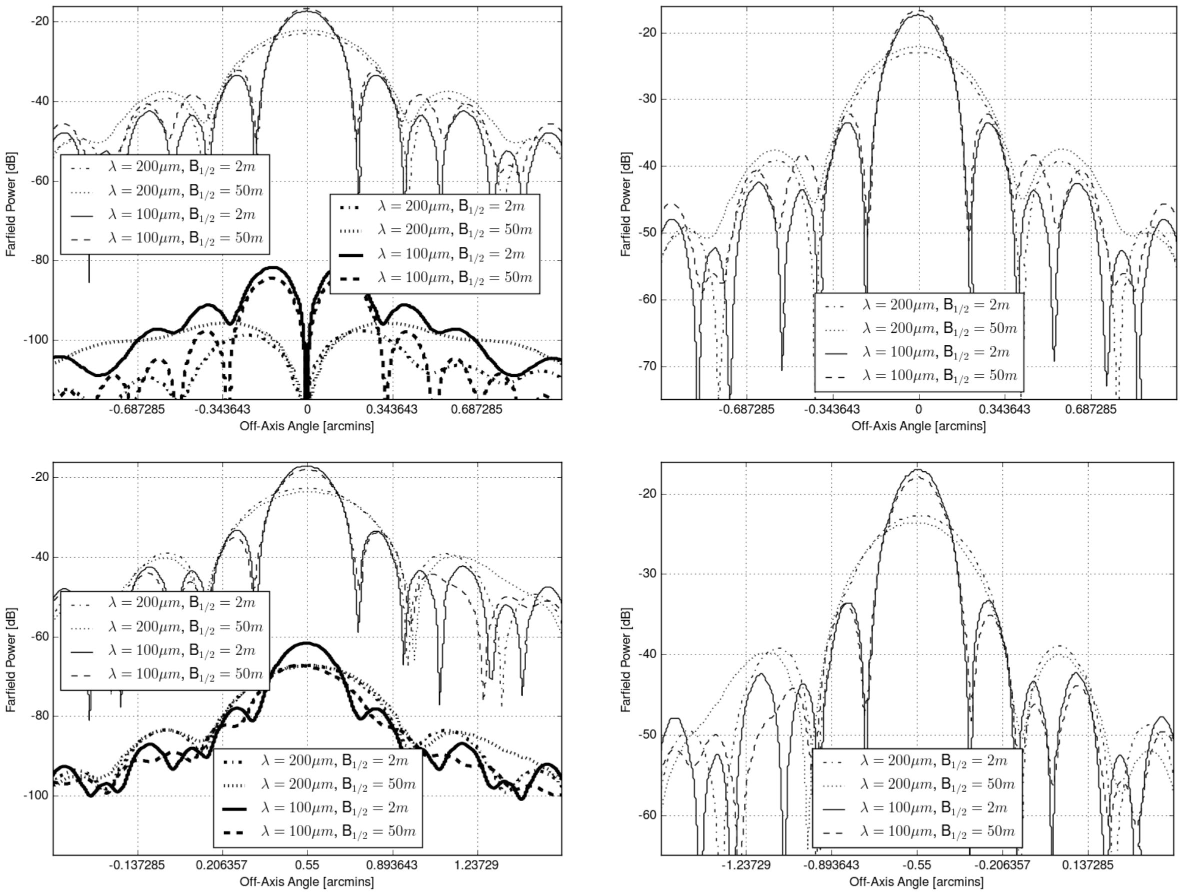

Figure 5: Far-field patterns for a single telescope illuminated by an on-axis (top) and furthest off-axis (bottom) feed horn, for a minimal semi-baseline of $B_{1/2} = 2$ m, and the maximum semi-baseline distance ($B_{1/2} = 50$ m). *Left*: Co-polar power E-plane cuts ($\phi = 0°$), and cross-polar power ($\phi = 45°$). *Right*: Co-polar power H-plane cuts ($\phi = 90°$), showing good beam symmetry when compared with E-plane cuts.

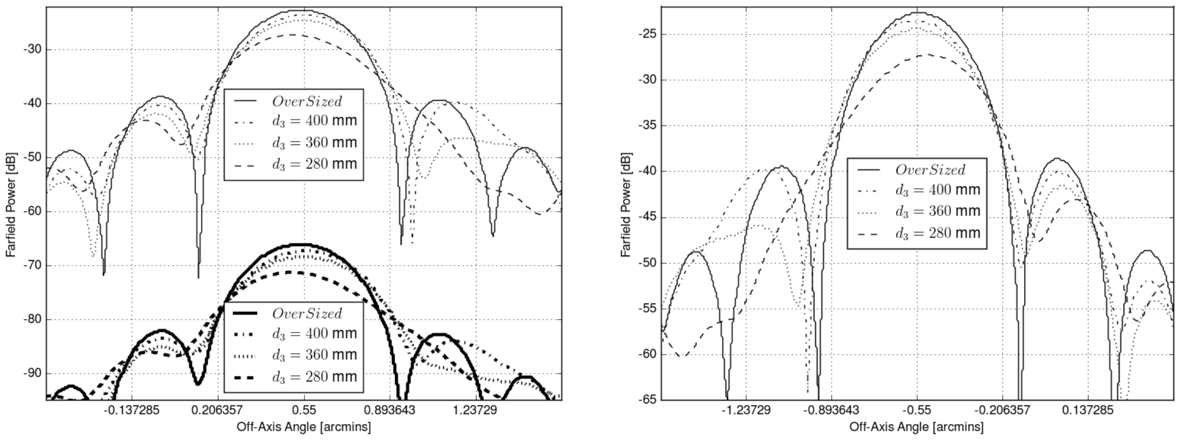

Figure 6: Far-field patterns for a single telescope illuminated by the furthest off-axis feed horn at $\lambda = 200$ μm, for the maximum semi-baseline ($B_{1/2} = 50$ m). In this case the diameter (d_3) of the hub primary mirror (M_3) was varied. Results for an over-sized mirror are shown for comparison. *Left*: Co-polar power E-plane cuts ($\phi = 0°$), as well as the cross-polar power ($\phi = 45°$). *Right*: Co-polar power H-plane cuts ($\phi = 90°$).

4.2. Fringe visibility

By examining cuts through the far-field interferometric beam patterns from the PO models, and comparing the central peak to the first trough, we can in some way interpret fringe (or interferometric) visibility for each of the pixels at a given wavelength using (3).

$$V = \frac{I_{max} - I_{min}}{I_{max} + I_{min}} \tag{3}$$

However, formulating a precise definition of fringe visibility becomes difficult for a FISICA-type system. As can be seen in Figure 7 (left) for an on-axis pixel and a relatively small baseline of 5 m, the visibility function falls off due to the beam envelope corresponding to the beam pattern of a single 2 m mirror. This is also the case for larger baselines, although it is difficult to see in Figure 7 (right) as the plot is zoomed-in due to the much finer resolution ($B = 50$ m). Furthermore, while the first troughs about the central peak do have minima of roughly zero, the troughs at larger angular separation do not quite reach zero. In fact the ‘local’ visibility degrades with increasing angular separation from the central peak, particularly for the largest baselines and shortest wavelengths. Thus, the question arises as to which peak/trough pair or combination should be used for calculating V? This brings to attention one of the particularly important benefits of having available an end-to-end instrument simulator such as PyFIInS. Rather than struggling with precise definitions of fringe visibility, we can instead generate realistic beam data similar to those shown in Figure 5, and allow PyFIInS to simulate the double-Fourier process for observation of a particular sky scene. The details of the re-constructed sky maps and spectra can then inform on the level of visibility.

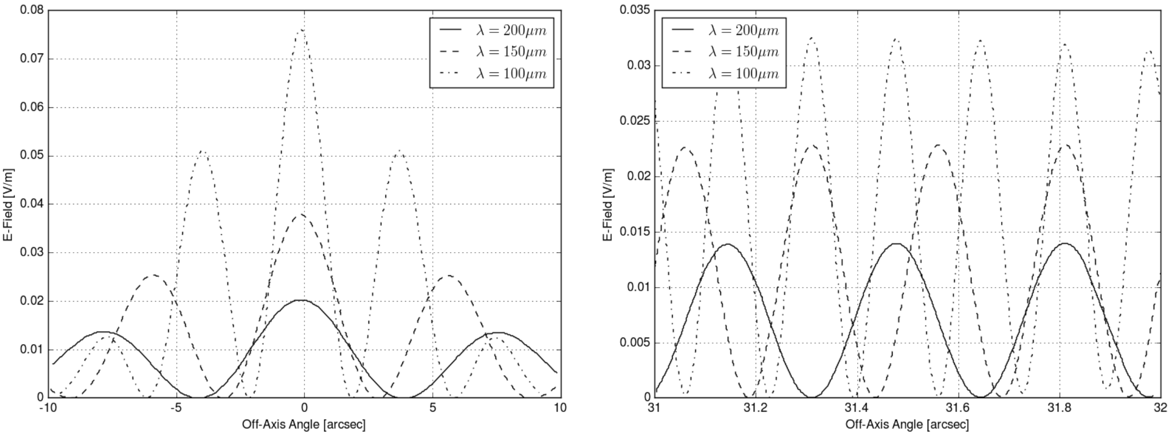

Figure 7: Cuts through far-field interferometric beam pattern for two 2 m telescopes. The left plot is for an on-axis single-mode horn antenna and a baseline of $B = 5$ m, giving resolutions of $\theta = 4''$ at 100 μm, and $\theta = 8''$ at 200 μm. The right plot is for an off-axis single-mode horn antenna and a baseline of $B = 50$ m, giving resolutions of $\theta = 0.4''$ at 100 μm, and $\theta = 0.8''$ at 200 μm, as would be expected.

5. Conclusions

A final design for a real system would largely depend on mass and volume limitations, and the allowable levels of wavefront error at the shortest wavelengths and beam truncation at the longest wavelengths. However, for a system capable of satisfying the requirements of the FISICA science case, such as that described above, the ideal de-magnification for the 2 m light collecting telescopes is about $m = 10$. A 5×5 array of single-mode detectors could be used to achieve the arcmin^2 FOV for band 3. Alternatively, a smaller array of over-moded horns or one large multi-mode horn could achieve the required FOV for band 3. The number of detectors required to fill the FOV for bands 1 and 2 would clearly be higher.

The design parameters shown in Table 2 result in a system capable of producing good predicted beam patterns on the sky for both on-axis and off-axis pixels, and for the large baselines demanded by the resolution requirements of FISICA. A relatively low level of beam truncation is apparent for the off-axis pixels of band 3, which results in a loss in gain of about 1 dB for the most off-axis pixels of the array. Throughput can be increased to above 99% for all pixels by increasing the diameter of the hub window to about 430 mm, although the size of the hub optics may well be the limiting factor in a real system.

It was shown that if a waveband 4 ($200 - 400$ μm) was to be included, then the optics in the central hub would be impractically large, unless a significantly reduced FOV is to be accepted. The physical optics analysis was only carried out for waveband 3 ($100 - 200$ μm), since the shorter wavelengths of wavebands 1 and 2 ($25 - 50$ μm, and $50 - 100$ μm, respectively) will be less affected by diffraction, etc. However, for analysis of wavefront error and the resulting loss in fringe visibility, the shorter wavelengths will be more critical. Thus, waveband 1 will be the focus of that future work. Other future work will focus on double-Fourier simulations with the PyFIInS instrument simulator and realistic beams.

Acknowledgements

This research has received funding from the European Union's Seventh Framework Programme (FP7/2007 - 2013) under FISICA grant agreement no. 312818. The corresponding author also acknowledges the Irish Research Council for providing additional funding for this work.

References

[1] F. Helmich, R. Ivison, FIRI - a far-infrared interferometer, Experimental Astronomy 23 (1) (2009) 245–276. doi:10.1007/s10686-008-9100-2.

[2] D. Leisawitz, et al., The space infrared interferometric telescope (SPIRIT): High-resolution imaging and spectroscopy in the far-infrared, Journal for Advanced Space Research 40 (1) (2007) 689–703. doi:10.1016/j.asr.2007.05.081.

[3] S. Rinehart, et al., The balloon experimental twin telescope for infrared interferometry (BETTII): An experiment for high angular resolution in the far-infrared, Publications of the Astronomical Society of the Pacific 126, (941) (2014) 660–673. doi:10.1086/677402.

[4] G. Savini, P. Ade, N. Baccichet, C. Bracken, et al., Progress in the critical assessment for a far-infrared space interferometer with double fourier modulation (FP7-FISICA), OSA Technical Digest, Optical Society of America Imaging FTS in Astronomy (FT4A) (2015) FT4A.3. doi:10.1364/FTS.2015.FT4A.3.

[5] V. Iafolla, E. Fiorenza, L. Iafolla, C. Lefevre, C. Magnafico, F. Santoli, L. Spinoglio, FISICA (far infrared space interferometer critical assessment) metrological problems and system requirements for interferometric observations from space, Proceedings of IEEE Metrology for Aerospace (MetroAeroSpace) (2014) 161–166. doi:10.1109/MetroAeroSpace.2014.6865913.

[6] M. Servillat, A. Coleiro, S. Chaty, F. Rahoui, J. Zurita-Heras, Herschel observations of dust around the high-mass x-ray binary gx 301-2, The Astrophysical Journal 797 (2) (2014) id. 114, 10 pp. doi:10.1088/0004-637X/797/2/114.

[7] I. Oteo, Dust correction factors over 0<z<3 in massive star-forming galaxies derived from a stacking analysis of herschel data, Astronomy and Astrophysics 572 (2014) id. L4, 12 pp. doi:http://dx.doi.org/10.1051/0004-6361/201424607.

[8] M. Werner, G. Fazio, G. Rieke, T. Roellig, D. Watson, First fruits of the spitzer space telescope: galactic and solar system studies, Annual Review of Astronomy and Astrophysics 44 (1) (2006) 269–321.

[9] J. Goicoechea, P. R. K. Isaak, L. Spinoglio, B. Swinyard, The SPICA assessment study report, Prepared by the ESA SPICA Study Team, the SPICA Telescope Science Study Team, the JAXA/ISAS SPICA Team and the SAFARI Consortium.

[10] N. Elias-II, N. Harwit, D. Leisawitz, S. Rinehart, The mathematics of double-Fourier interferometers, The Astrophysical Journal 657 (2) (2007) 1178–1200. doi:10.1086/510878.

[11] R. Juanola-Parramon, A far-infrared spectro-spatial space interferometer. instrument simulator and testbed implementation, Ph.D. thesis, UCL (University College London), phD Thesis (2014).

[12] J. Lightfoot, R. Juanola-Parramon, G. Savini, FIInS - a python simulator for a far-infrared double fourier interferometer in space, OSA Technical Digest, Optical Society of America Hyperspectral Imaging and Sounding of the Environment (JM3A) (2015) JM3A.9. doi:10.1364/FTS.2015.JM3A.9.

[13] L. Spinoglio, D. Schito, S. Pezzuto, W. Holland, on behalf of the FP7-FISICA Consortium, D1.1: Definition/update of key science questions and relevant data products, FP7-FISICA Consortium.
URL `http://www.homepages.ucl.ac.uk/ ucapgsa/Test`$_{d}ocs/D1.1_{s}ubmitted.pdf$

[14] C. Bracken, on behalf of the FP7-FISICA Consortium, Optical and quasi-optical analysis of system components for a far-infrared space interferometer, Proceedings of SPIE 9362 Terahertz, RF, Millimeter, and Submillimeter-Wave Technology and Applications VIII (93620N) (2015) 12 pp. doi:10.1117/12.2076385.

[15] E. C. D. Facility, FIRI - far infrared interferometer, CDF Study Report CDF-49(A) (2006) 130–131.

[16] P. Goldsmith, Quasi-optical techniques, Proceedings of the IEEE 80 (11) (1992) 1729–1747. doi:10.1109/5.175252.

[17] A. Poglitsch, et al., The photodetector array camera and spectrometer (PACS) on the herschel space observatory, Astronomy and Astrophysics 518 (L2) (2010) id. L2, 12 pp. doi:10.1051/0004-6361/201014535.

[18] M. J. Griffin, et al., The herschel-SPIRE instrument and its in-flight performance, Astronomy and Astrophysics 518 (L3) (2010) id. L3, 7 pp. doi:10.1051/0004-6361/201014519.

[19] N. Trappe, et al., Quasi-optical analysis of the HIFI instrument for the Herschel Space Observatory, Proceedings of SPIE 4876 Optics and Photonics Technologies and Applications (1091). doi:10.1117/12.463910.

[20] W. Jellema, et al., The optical design concept of SPICA-SAFARI, Proceedings of SPIE 8442 Space Telescopes and Instrumentation 2012: Optical, Infrared, and Millimeter Wave (84420S) (2012) id. 84420SI, 9 pp. doi:10.1117/12.927153.

[21] H. Matsuhara, et al., Cooled scientific instrument assembly onboard SPICA, Proceedings of SPIE 8442 Space Telescopes and Instrumentation 2012: Optical, Infrared, and Millimeter Wave (84423U) (2012) id. 84423U, 11 pp. doi:10.1117/12.926984.

[22] K. Pontoppidan, GRASP technical description, TICRA.

[23] M. Audley, et al., Optical measurements of TES bolometers for SAFARI, Proceedings of 23rd International Symposium on Space Terahertz Technology 2012 (2012) 189–197.

[24] S. Doyle, et al., Lumped element kinetic inductance detectors, Journal of Low Temperature Physics 151 (1) (2008) 530–536. doi:10.1007/s10909-007-9685-2.

[25] C. Aime, E. Aristidi, Y. Rabbia, The fresnel diffraction: A story of light and darkness, New Concepts in Imaging: Optical and Statistical Models, EAS Publications Series 59 (2013) 37–58. doi:10.1051/eas/1359003.

[26] J. Murphy, A. Egan, Examples of fresnel diffraction using gaussian modes, European Journal of Physics 14 (3) (1993) 121–125. doi:10.1088/0143-0807/14/3/005.

[27] Y.-L. Xu, Fraunhofer diffraction of electromagnetic radiation by finite periodic structures with regular or irregular overall shapes, Journal of the Optical Society of America A 32 (1) (2015) 12–21. doi:10.1364/JOSAA.32.000012.